PCCP

Accepted Manuscript

ARTICLE

Spatial Frequency Heterodyne Imaging of Aqueous Phase Transitions inside Multi-walled Carbon Nanotubes

F. M. Schunk,[a] D. Rand[b] and C. Rose-Petruck[c*]

The evaporation and condensation of water on multi-walled carbon nanotube (MWCNT) surfaces was studied as a function of temperature and time using X-ray Spatial Frequency Heterodyne Imaging (SFHI). SFHI is an imaging modality that produces an absorption and scatter image in a single exposure, and has increased sensitivity to variations in electron density relative to more common place X-ray imaging techniques. Differing features exhibited in the temporal scatter intensity profiles recorded during evaporation and condensation revealed the existence of an absorption-desorption hysteresis. Effects on the aforementioned phenomena due to chemical functionalization of the carbon nanotube surfaces were also monitored. The increased interaction potential between the functionalized MWCNT walls and water molecules altered the evaporation event time scale and increased the temperature at which condensation could take place. Theoretical calculations were used to correlate the shape of the observed scatter profiles during condensation to changes in the MWCNT cross section geometry and configuration of the contained water volume. Changes in evaporation time scales with temperature coincided with the boiling point for confined water predicted by the Kelvin equation, indicating that a thermodynamic description of mesoscopic confined water is permissible in some instances.

Introduction

The spatial dimensions of nanomaterials bestow on them unique properties, and fluids confined at the nanoscale show properties that differ from the bulk[1-3]. Evaporation and condensation of water confined to the inner cavity of carbon nanotubes (CNTs) was the focus of this study. Understanding of fluids confined to nano dimensions is necessary to facilitate widespread application of nanofluidic phenomena to fields including transmembrane transport[4], sequestration of gases in nanoporous minerals[5], nanofluidic devices[6], chromatography[7], and water purification[8].

Dujardin *et. al.*[9] demonstrated that CNTs are wetted by liquids of interfacial tension below 200 mN/m. Water has an interfacial tension of approximately 72 mN/m and therefore wets CNTs despite their insolubility in polar solvents[10]. The acute contact angle water makes with CNT surfaces permits population of the inner cavity via capillary forces. Functionalization of the CNT surfaces by oxidation decreases the contact angle of water by addition of oxygen containing functional groups,[11] exaggerates defect sites, and removes any hemispherical caps possibly sealing the CNTs at either

a. Department of Chemistry Brown University, 324 Brook St. Providence, RI 02912, USA.
b. Department of Chemistry Brown University, 324 Brook St. Providence, RI 02912, USA.
c. Department of Chemistry Brown University, 324 Brook St. Providence, RI 02912, USA.
† * Corresponding author.
Electronic Supplementary Information (ESI) available: [Data including error bars]. See DOI: 10.1039/x0xx00000x

end.[12-14] Barber *et. al.*[15] obtained estimates for the contact angles water makes on the inner and outer surfaces of carbon nanotubes, and found that the inner contact angle is smaller than the external contact angle.

Capillary theory predicts a decrease in water vapor pressure within CNTs resulting from formation of an aqueous meniscus with negative radii of curvature. An increased boiling point is an immediate consequence of decreased vapor pressure. The Kelvin equation

$$RTln\left(\frac{P}{P_o}\right) = v\gamma(\frac{1}{R_1} + \frac{1}{R_2}),\qquad(1)$$

predicts the change in vapor pressure of a liquid as its free surface deviates from a planar geometry, and the Clausius-Clayperon equation yields the change in boiling point given the change in vapor pressure. In the above equation R is the gas constant, T is the temperature in Kelvin, P is the vapor pressure above the meniscus, P_o is the vapor pressure above a planar surface, v is the molar volume of the liquid, γ the liquid interfacial tension, and the menisci's principle radii of curvature are R_1 and R_2. Molecular dynamics simulations have also shown that pressures on the order of hundreds of bar are possible by heating water confined to a closed CNT within a few tens of degrees above its boiling point[16]. The ability to generate such high pressures by relatively mild heating could have a dramatic impact on the high pressure chemical industry.

The specific manner in which water condenses into a rigid cylindrical capillary was proposed in a model by Everett and Haynes[17] in which water first adsorbs onto the inner surface forming a thin film. Further condensation promotes the formation of an unduloidal liquid surface until the surface possesses an effective surface area greater than that of a meniscus configuration. At this liquid volume the unduloidal surface collapses to a lens shaped meniscus. The lens then grows towards the ends of the capillary as condensation continues. Using environmental scanning electron microscopy (ESEM) Rossi *et. al.*[18] observed a series of liquid configurations during the adsorption of water into 200 nm diameter CNTs that follows the predictions of Everett and Haynes. A change in CNT cross section geometry was also observed to accompany the different stages of filling. A radial contraction of the CNTs occurred with the formation of a liquid thin film. The CNTs then took on an elliptical cross section upon formation of a lens shaped meniscus, and regained their original circular cross section when the inner pore was completely filled with a planar meniscus at each end.

The confinement of water to CNT pores and its evaporation and condensation from them has been observed by nuclear magnetic resonance[19] (NMR), X-ray diffraction[20, 21] (XRD), transmission electron microscopy[22] (TEM), and ESEM. NMR, TEM, ESEM, and XRD suffer from limitations with respect to studying large samples composed of large particles. Owing to the complex nature of the information obtained from its spectra NMR cannot be successfully applied to molecules with mass greater than a few tens of kilodaltons without the use of transverse relaxation-optimized spectroscopy[23]. TEM only probes small samples (at most a few CNTs) of a population, and studies in aqueous environments are prohibited by the necessity to image under high vacuum. ESEM is not limited by a high vacuum environment but is still only capable of probing small samples. XRD measures the atomic structure of a sample but does not probe its mesoscopic structure. For instance, shape changes of CNTs or the average density of the water enclosed are difficult to deduce from XRD patterns. Diffraction experiments

probe a large sample volume compared to TEM and ESEM but are only of sub-millimeter size. Larger sample areas require scanning the sample through a collimated x-ray beam. As a consequence a sample under study and its reference cannot be observed simultaneously.

Small-angle x-ray scattering (SAXS) is sensitive to mesoscopic structure revealing particle size, shape, and orientation but requirement of a collimated x-ray beam limits sample size as in the case of XRD. SFHI, the imaging technique employed in this study, relies on the elastic scattering of x-rays into small angles but permits the imaging of arbitrarily large samples. SFHI is accomplished by placing an x-ray source, absorption grid, object, and detector in tandem (Figure 1) to generate images composed only of radiation scattered through small angles by the object[24]. The detected intensity is composed of transmitted and diffracted intensities by the object and grid. Scattering due to the object effectively blurs what would be a crisp grid projection onto the detector. Fourier analysis methods are then implemented to extract a measure of the grid blurring and therein scatter from the object.

The Fourier transform of the recorded image is taken to generate the grid and object reciprocal space. The grid produces a regular lattice of points located at its spatial frequency harmonics, and the spatial frequency spectrum of the object is replicated about each point. This can be understood in the limit of no scattering. If the grid and sample do not scatter radiation the detected image is a product of their transmitted intensities, which is a convolution in Fourier space. In this scenario all of the harmonic peaks are identical. Due to the general decay of scattering factors with increasing spatial frequency higher harmonics are attenuated by scattered radiation. Attenuation of amplitudes at higher spatial frequencies away from those due to transmission is utilized to extract a signal proportional to the integrated scatter intensity. The modulus of the angular spatial frequency $\vec{q}$ is related to the scattering angle by

$$|\vec{q}| = \frac{4\pi \sin\theta}{\lambda},\qquad(2)$$

where θ is one half of the scattering angle and λ is the wavelength of the incident radiation. The use of a two dimensional absorption grid allows scatter into those two dimension to be distinguished, making SFHI sensitive to sample anisotropy.
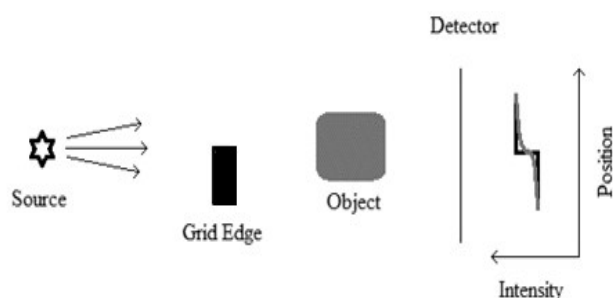
Figure 1: Schematic of SFHI imaging system. Radiation scattered by the object blurs the contrast of the grid projection. The intensity profile of the un-blurred grid projection is shown at the far right in black, and its projection blurred by scatter from the object is shown in grey. The item labelled grid edge should be seen as a cross section of a single wire in the two dimensional wire mesh that is actually used to carry out experiments.

The harmonics are multiplied by low pass filters, individually inverse Fourier transformed, and normalized by the corresponding image from an exposure of the grid alone in order to generate a harmonic image. The central harmonic yields a conventional absorption image, because those spatial frequencies correspond to near zero scattering angles and are therefore indistinguishable from transmitted radiation. This image is referred to as the absorbance or (0,0) image. A scatter image is produced by taking the ratio of an image produced from a higher harmonic to the absorbance image. Figure 2 depicts a schematic of the image processing. More thorough explanations may be found elsewhere[24-26].

SFHI's reliance on SAXS makes it ideal for investigating nanoscale objects[27], which is a short coming of NMR and XRD. SFHI does not require a special environment permitting the study of aqueous phase transitions, which is impossible with TEM. ESEM has been used to directly observe the phenomena investigated in this paper, but the observations were made for CNTs on a much larger size scale and only for a single CNT. Direct imaging of phenomena on the nanoscale by ESEM is invaluable but it does not lend itself readily to making quantitative time resolved measurements, while the intensities of SFHI scatter images hold deeper physical significance. SFHI time resolved imaging capabilities have been demonstrated by imaging gas formation accompanying the carbon steam reaction of carbon nanoparticles in water after laser-pulse heating.[28] Also traditional SAXS requires the use of a synchrotron, where SFHI can be performed with a commercial X-ray tube. Previous studies have shown SFHI to have greater sensitivity to iron oxide[29] and gold[30] nanoparticle contrast agents than absorption radiography.

Experimental

MWCNTs with an inner diameter of 7 ± 2 nm, an outer diameter of 15 ± 5 nm, and a length of 1-5 μm produced by chemical vapor deposition were obtained from Nano Lab Inc. (Waltham, MA). The synthesis closely followed that of Ren *et. al.*[31]. A fraction of the MWCNTs were placed in a Pyrex tube open to atmosphere and heated to 500° C for approximately 50 minutes in order to functionalize the CNTs. Heating produced a 15% mass loss.

Two functionalized and two as-purchased 16 mg samples of MWCNTs were placed in glass tubes. The CNTs were packed at one end of the glass tubes by a glass wool plug, and 250 μl of nano-pure water were added to one functionalized and one as-purchased sample. All four samples were then vacuum sealed and placed in an aluminum holder fitted with two heating elements, a thermocouple, and five sample slots. The middle slot contained an
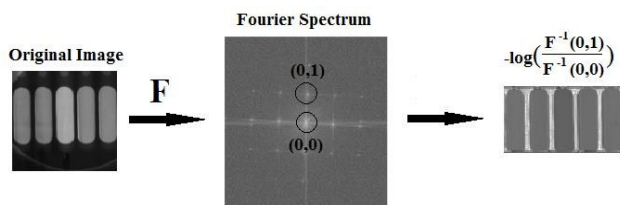

Figure 2: Schematic of image processing. The image on the left is an exposure of glass tubes containing CNTs in an aluminium holder. This image is then Fourier transformed to generate the reciprocal space (middle). The central (0,0) and first vertical (0,1) spatial frequency harmonics are enclosed in the circumference of low pass filters that would be applied in the image formation algorithm. Then inverse transforms of the (0,1) and (0,0) harmonics are taken and used to generate real images. The negative logarithm of their ratio gives the scatter image (right) corresponding to the higher harmonic.
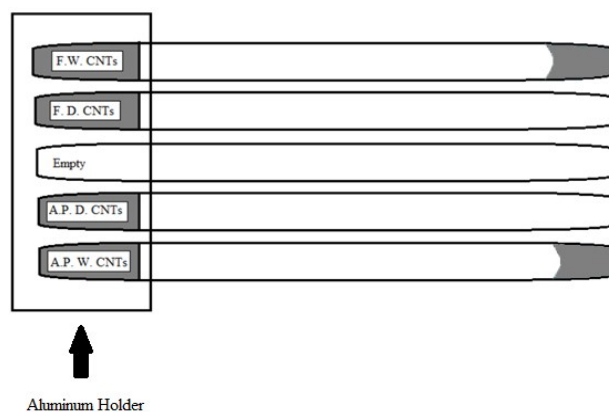

Figure 3: Sample holder schematic. F. W. and F. D. stand for functionalized wet and functionalized dry respectively. A. P. W. and A. P. D. stand for as-purchased wet and dry respectively. The CNT samples are contained within the dimensions of the aluminium holder, and water droplets are depicted at the far ends of the glass tubes for the wet samples.

empty glass tube. The two samples that did not have water explicitly added were heated to 110 °C for ten minutes while under vacuum in order to insure that all water already adsorbed into the CNTs was removed. The portions of the glass tubes containing CNTs were within the dimensions of the holder, while the empty lengths of glass tubing that remained extended beyond the holder. Extension beyond the dimensions of the aluminum holder allowed the vacant portion of the glass tubes to remain at room temperature throughout the experiment. The dry samples were therefore under vacuum while the wet samples were under a pressure equal to that of water vapor pressure at room temperature. A schematic of the holder is presented in Figure 3.

The holder was placed 1.2 m below a 12 bit remote RadEye 200 CMOS detector in a vertical imaging arrangement with a 1.6 m source to detector distance. The source was a True Focus X-ray tube, model TFX-3110EW with a Tungsten anode and 10 μm focus size. The tube was operated at 80 KV and 0.2 mA. The absorption grid was a two dimensional 150 line per inch stainless steel wire mesh with 0.0026 inch gauge. The grid was placed immediately below the sample holder. Only the sample volumes contained within the dimensions of the aluminum holder were in the viewing field of the imaging system. As the samples were heated a temperature gradient was established and water condensed at the room temperature end of the glass tubes out of the viewing field.

Prior to imaging the samples were situated in a vertical position to ensure contact of the CNTs with the added water. The samples were then oriented horizontally and heated to 80° C for 30 minutes to expel excess water from the samples into the region of the glass tubes outside of the viewing field. After preheating the samples were allowed to cool for four hours.

Two separate experiments were conducted using the prepared samples. In the first experiment the samples were heated as quickly as possible to a set point temperature that was then maintained. The set points covered were 45 °C, 60 °C, 85 °C, and 95 °C. Equilibration at the set points never took longer than three minutes. In the second experiment both evaporation of water from the samples and condensation of water back into the samples were monitored by application of a 1 hour heating ramp to 320 °C followed by a cooling period where the samples radiated heat. In both experiments sets of 5 exposures 10 seconds in length were taken at regular intervals between temperature measurements.

Scatter images were then produced by processing the recorded exposures.

The spatial harmonics were multiplied by a 14th order Butterworth Hann hybrid filter,

$$
w = \begin{cases} \left[1 + \left(\frac{|\vec{q}|}{|\vec{q}_0|}\right)^n\right]^{-\frac{1}{2}}, & |\vec{q}| < |\vec{q}_0|3^{\frac{1}{n}} \\[2mm] \left[1 + \left(\frac{|\vec{q}|}{|\vec{q}_0|}\right)^n\right]^{-\frac{1}{2}} * \left[\frac{1}{2} + \frac{1}{2}cos\left(\frac{\pi|\vec{q}|}{|\vec{h}_0|}\right)\right], & |\vec{q}| \geq |\vec{q}_0|3^{\frac{1}{n}} \end{cases}. \quad (3)
$$

In the above equation w is the filter/window function, $|\vec{q}|$ is the spatial frequency relative to the harmonic of interest, $|\vec{q}_0|$ is the spatial frequency at which the Butterworth filter attenuates the gain to 70.7 percent of the maximum, n is the Butterworth filter order, $|\vec{h}_0|$ is the spatial frequency at which the Hann filter attenuates the gain to zero, and $|\vec{q}_0|3^{\frac{1}{n}}$ is the spatial frequency at which the Butterworth filter attenuates the gain to 50 percent of the maximum. The Butterworth cutoff frequency $|\vec{q}_0|$ was chosen as 40 percent of the inter-harmonic distance, and the Hann cutoff frequency $|\vec{h}_0|$ was chosen as 50 percent of the inter-harmonic distance.

The Gibbs phenomena refers to the Fourier series of a piecewise smooth discontinuous function exceeding the function's limiting value at a jump discontinuity. The Gibbs phenomena results in oscillations of the function's Fourier series, and these oscillations are a source of ringing in data processing. Gibbs phenomena is associated with the Fast Fourier Transform of a function that has been multiplied by a window function or filter, and is therefore an issue that must be addressed in the current work The hybrid filter used minimizes the degradation of image spatial frequency integrity and ringing due to Fast Fourier transformation better than either individual filter. Higher spatial frequencies relative to a given harmonic become less attenuated as the Butterworth filter order increases, and in the limit of infinite order a radially symmetric Butterworth filter is equal to a right cylindrical filter and produces a jump discontinuity. So if the Butterworth order is made too high the attenuation of spatial frequencies within the filter domain is minimized, but the rate of gain attenuation at the filter boundaries is sufficiently similar to a jump discontinuity that ringing may be observed in the resultant images. The order of the Butterworth filter was chosen to be as large as possible without re-introducing the Gibbs phenomena that would result from a simple right cylindrical shaped filter. The Hann function's contribution to the filter forces the window function to smoothly decay to zero avoiding ringing produced by a jump discontinuity as a result of truncating the window function at some spatial frequency.

Average intensities were measured over pixel subsets of the images contained within the sample regions, and a further average was taken over each set of five exposures. Only the first vertical harmonic was used, because the edges of the aluminum holder and glass tubes were aligned vertically in the images causing the horizontal harmonics to contain scatter from these features. The difference in average intensities between samples containing water and their corresponding dry sample were taken to correct for any change in the detector sensitivity.

Results

The absolute intensities recorded have little physical significance compared to the change in intensity with time, because the intensities detected are a function of photon flux, the analogue to digital conversion process, and contain transmitted and scattered radiation from the aluminum holder and glass tubes. Figure 4 contains the results of heating the samples to various set point temperatures. In the legend F refers to the samples that were functionalized by heat treatment, and AP refers to the as-purchased samples. The signals depicted are the differences between the intensities measured for the samples containing water and their corresponding dry samples, so any change in intensity is due solely to the effect of added water. The abscissa was normalized to the time at which all water had been removed from the as-purchased CNTs. The time in hours to which the abscissa was normalized is located next to the temperature at which images were collected.

The left ordinate is the scale for image intensities obtained from the (0,0) harmonic, so these intensities are due to changes in absorption and have been rescaled to represent the amount of water in the samples as a percentage of the initial water content. A rescaling of absorbance values is permissible because absorbance is proportional to concentration. No such rescaling is permissible for the integrated scatter intensities, whose scale is the right ordinate. Scattered intensity is only related to the number of scattering centers squared in the zero scattering angle limit. Both the scatter and absorbance intensities were offset corrected.

In each of the four graphs shown in Figure 4 the absorbance intensities decrease monotonically in accord with water leaving the viewing field. The integrated scatter intensity profiles for the functionalized and as-purchased samples are qualitatively the same at each temperature with an initial increase in intensity, followed by a subsequent increase, and then decrease back to baseline. A change in integrated scatter intensity for both samples is not observed until 20 to 30 percent of the water has been evaporated from the CNTs, indicating that unlike absorbance the scatter intensity is not sensitive to the change in water content alone. At 45 °C (Figure 4 **a**) and 60 °C (Figure 4 **b**) water starts to evaporate from the as-purchased sample at an earlier time than the functionalized sample, and at 85 °C (Figure 4 **c**) and 95 °C (Figure 4 **d**) water starts to evaporate from the as-purchased and functionalized samples at about the same time. At all temperatures regardless of when evaporation begins water leaves the functionalized samples at a faster rate. Table 1 contains ratios of the slopes obtained from linear fits of the absorbance signals from 0.2 to 0.5 normalized time at each temperature. The change in evaporation rates between the functionalized and as-purchased samples with temperature is clearly seen in the absorbance profiles, but is also dramatized by the displacement of the scattering profiles relative to one another. At 85 °C and 95 °C the increased evaporation rate of water from the functionalized sample compresses the scatter intensity profiles in time relative to the as-purchased sample.

Figure 5 contains the results of the second experiment where the CNTs were heated and then allowed to cool. The absorbance signals for both samples again monotonically decrease as water leaves the viewing field upon heating, and monotonically increase during condensation. Condensation occurred at about 70 °C in the functionalized sample and 40 °C in the as-purchased sample. The integrated scatter profiles during heating are similar in shape to those found in the experiments conducted at different set point temperatures except that they are compressed in time due to the rapid heating rate. During condensation the as-purchased scatter profile has a peak like shape while the functionalized scatter profile merely shows an abrupt increase. The difference between the two scatter signals is due to a lack of control over the degree of filling.
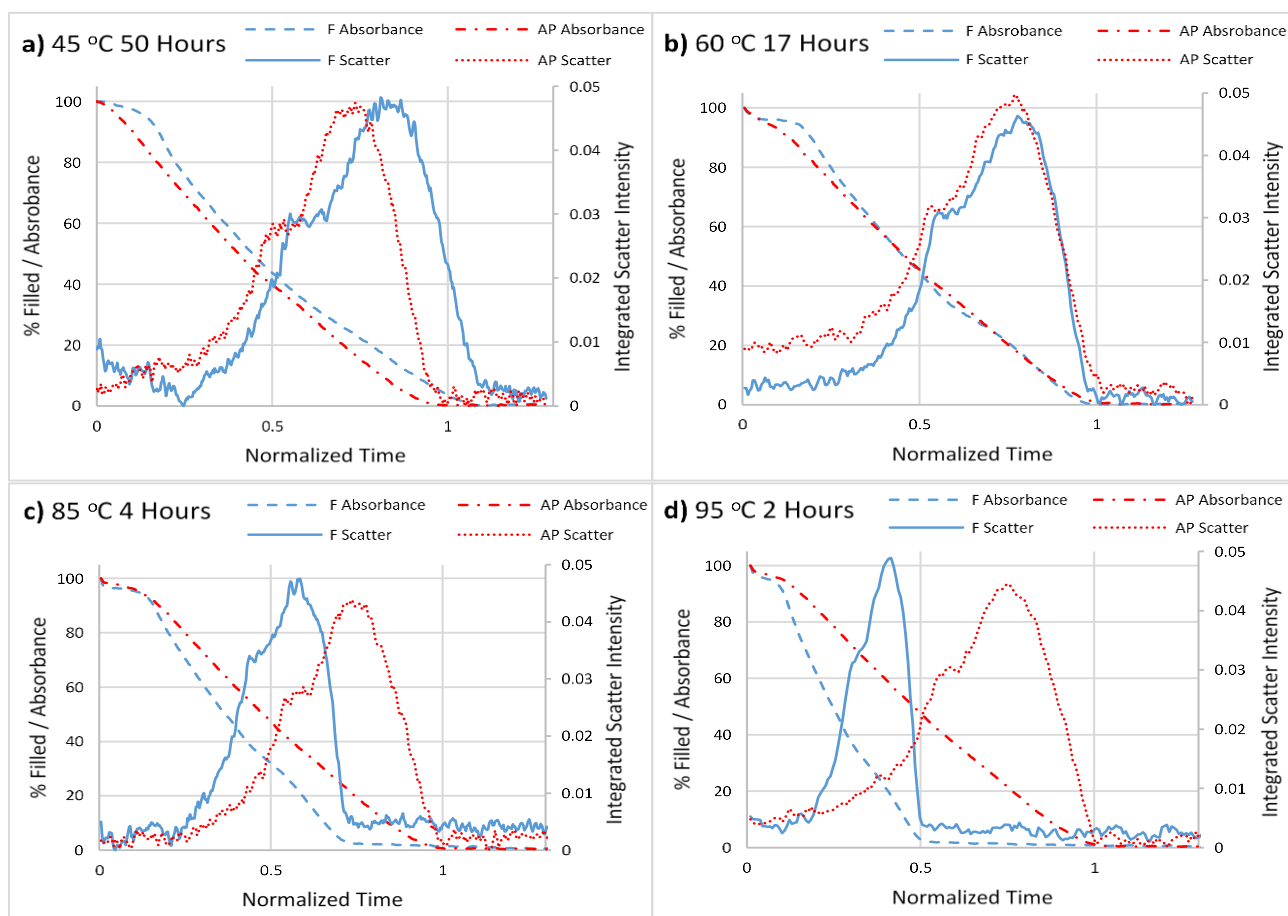
Figure 4: The samples were heated to different temperatures which were then maintained. It never took longer than three minutes to achieve thermal equilibrium at the set point temperature. The absorbance intensities have been rescaled and offset correct to represent the degree of water filling as a percentage of the initial water content. The integrated scatter intensities are offset corrected. In the legends F stands for the samples that were functionalized by heat treatment, and AP stands for the as-purchased samples. The CNTs were heated to 45 ⁰C (**a**), 60 ⁰C (**b**), 85 ⁰C (**c**), and 95 ⁰C (**d**) after having been oriented vertically so any water in the samples soaked the CNTs. The abscissa has been normalized to the time at which evaporation went to completion in the as-purchased sample. The time to which the abscissa was normalized is located next to the temperature at which the experiment was conducted. All signals depicted are the differences between the wet samples and their corresponding dry samples. The relative error for a 95% confidence interval was never greater than 4% of the signal amplitude for all curves displayed.

Discussion

Functionalization of the CNTs by oxidation served to delay the evaporation of water from the inner pore of the CNTs at low temperatures, and to increase the temperature at which adsorption could take place. Evaporation from the functionalized sample is not seen to progress to any significant extent until 5 hours after the start of the experiment conducted at 45 ⁰C (Figure 4 **a**). Such a long period of time precludes the conclusion that the samples are not at thermal equilibrium leaving only the presence of functional groups as the cause for delayed evaporation.

At elevated temperatures the augmented interaction of the functionalized CNTs with water is overcome by increased thermal energy, and water from both the functionalized and as-purchased samples starts to evaporate at the same time. The increased evaporation rate from the functionalized sample seen at all temperatures (Table 1) is caused by uncapping of the CNTs and exaggeration of wall defects allowing for the escape of a larger number of water molecules per unit time. At temperatures where evaporation has gone to completion water vapor incident on the CNT surfaces constantly adsorbs and desorbs. When the samples

were allowed to cool the presence of polar functional groups on the oxidized CNT surfaces permitted permanent adsorption at a higher temperature relative to the as-purchased CNTs.

In an effort to interpret the shape of the scatter intensity profiles in terms of CNT shape and water content the integrals over SAXS distributions corresponding to the four states of CNTs observed in reference 18 were calculated. Figure 6 depicts the CNT model states used to compute SAXS distributions, and Figure 7 contains the results of taking the integral over each calculated distribution. The series of states modeled represent different instances along the progression of capillary condensation. The CNTs were modeled as 10 nm long tubule segments with electron densities taken as that of bulk material. The integrals over SAXS distributions corresponding to CNTs of constant cross section undergoing capillary condensation, and CNTs of changing cross section without capillary condensation were also calculated. The SAXS distribution for a statistically homogeneous object of random orientation is equal to the Fourier transform of the average electron density autocorrelation function,

$$I = \int_{-\infty}^{+\infty} \langle \mathcal{P} \rangle e^{-i\vec{q}\cdot\vec{x}} d\vec{x}, \qquad (4)$$
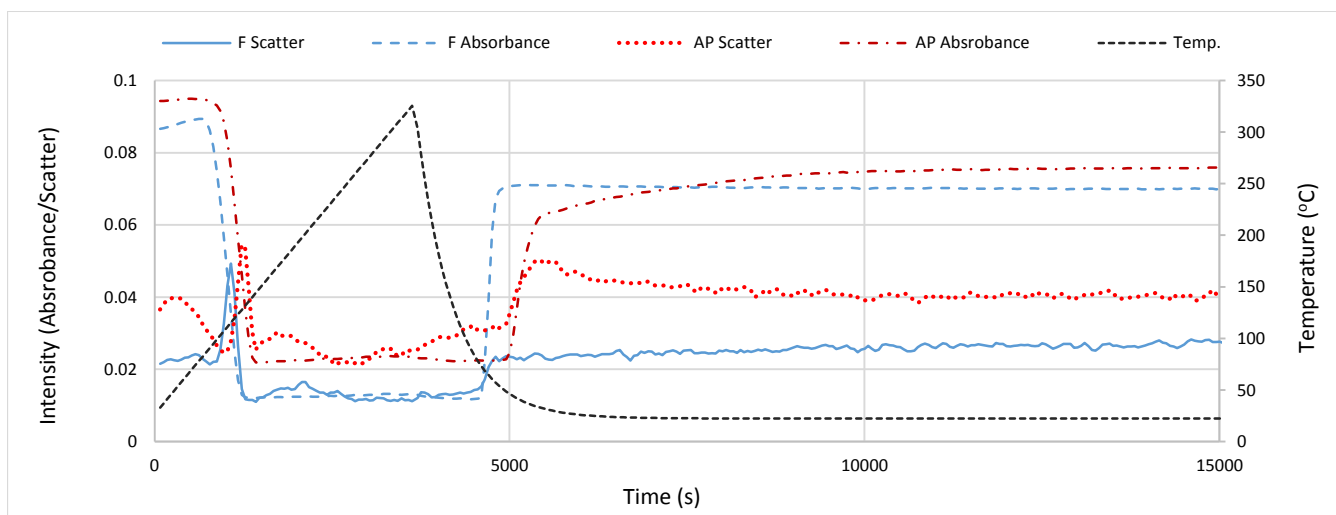
where

Figure 5: A one hour heating ramp to 320 °C and subsequent cooling period were applied to the samples. F and AP stand for functionalized and as-purchased respectively. Both the absorbance and integrated scatter signals are the differences between the wet samples and their corresponding dry samples. The relative error for a 95% confidence interval was never greater than 14% of the signal amplitude for all curves displayed.

$$\mathcal{P}(\vec{x}) = \int_{-\infty}^{+\infty} \rho(\vec{u})\rho(\vec{u} + \vec{x})d\vec{u}. \tag{5}$$

In equation 4 I is the scatter intensity distribution, $\mathcal{P}$ is the electron density autocorrelation function, the angled brackets indicate averaging over rotational orientation, the angular spatial frequency vector is denoted by $\vec{q}$, and $\vec{x}$ is the object space position vector. In equation 5 ρ is the electron density of the diffracting body, and $\vec{u}$ is a displacement vector. Equations 4 and 5 are in general true. That is they apply to both small and wide angle X-ray scattering. In small angle X-ray scattering the electron density is taken as constant over regions of the diffracting body practically ignoring the underlying atomic structure, whereas in wide angle scattering the electron density function does contain information about the atomic nature of the sample. In wide angle scattering equation 5 is termed the Patterson function.

The relations between the coordinates of points in an orthonormal right handed coordinate system rotated through the Eulerian angles relative to the coordinates of points in a fixed

orthonormal right handed coordinate system were used in conjunction with a series of branching statements to generate the relevant electron density functions for each CNT model state

$$\xi_i = \xi_i(\xi_1', \xi_2', \xi_3', \theta, \varphi, \psi), \ i = 1,2,3. \tag{6}$$

Equation 6 expresses the ith coordinate of a point in the original un-rotated coordinate system, ξ_i, as a function of the three coordinates of the corresponding point in the rotated coordinate system, ξ_1', ξ_2', ξ_3', and the three Eulerian angles, θ, φ, ψ. The exact functional form of these relations may be found in most texts on vector and tensor analysis. The above expression was used to map the coordinates of each point of a rotated coordinate system whose orientation was specified by a given permutation of the three Euler angles back to the original un-rotated coordinate system. If the point in the rotated system corresponded to a point in the un-rotated system that resided within the volume of the assumed CNT
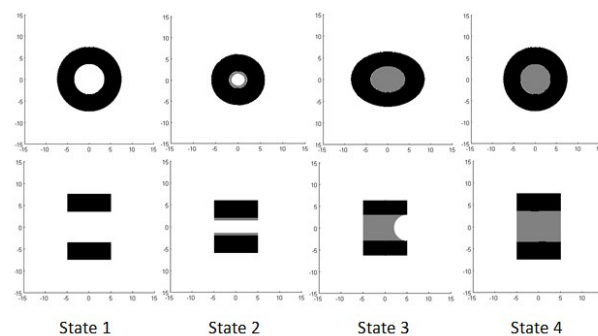
Temperature (°C)	Slope F / Slope AP	Slope AP (% Filled / Normalized Time)
45	1.079	-124.2
60	1.208	-120.88
85	1.233	-132.14
95	1.500	-123.66

Table 1: The ratios represent the relative evaporation rate of the functionalized sample with respect to the as-purchased sample at the different set point temperatures. The slopes used to compute the evaporation rate ratios were obtained from linear fits of the % filled signals in Figure 4 between 0.2 and 0.5 normalized time. The functionalized sample possesses an evaporation rate greater than that of the as-purchased sample at all temperatures.

Figure 6. State 1 is an empty CNT with circular cross section. State 2 shows the CNT after a 20% radial contraction caused by the formation of 1 nm thick film of water. State 3 shows an elliptical cross section resulting from a 10% change in radius along both the semi major and minor axes, following the formation of an aqueous meniscus. State 4 shows the CNT with its original cross section and complete filling with a planar menisci at both ends. The CNT was taken to be 10 nm in length. The CNT electron density was adjusted for each state such that the total number of electrons was held constant.
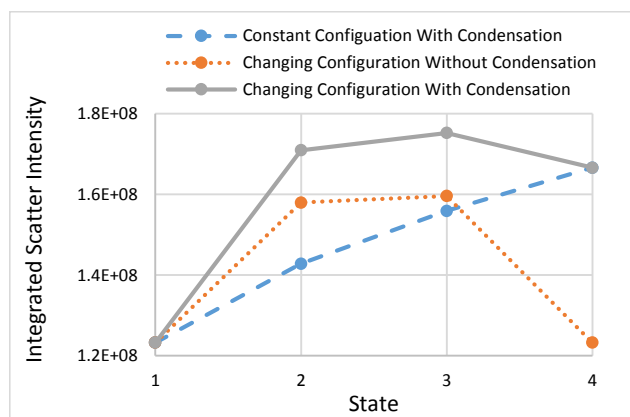
Figure 7. SAXS distributions were calculated for CNT models, and then integrated in an effort to interpret the recorded integrated scatter signals in terms of CNT geometry and water content. The states on the abscissa correspond to those described in Figure 6 for the CNTs with changing cross section and capillary condensation. Going from state 1 to state 4 corresponds to condensation of water into the CNTs, while going from state 4 to state 1 corresponds to evaporation of water from the CNTs. The model states of the series labeled *Changing Configuration Without Condensation* are exactly those depicted in Figure 6 without any water occupying the inner CNT pore. The model states of the series labeled *Constant Configuration With Condensation* all have CNT cross section geometry identical to that of state 1 in Figure 6 but fill with water according to the observations of reference 18. The series of model states with constant cross section undergoing condensation is most representative of Everett and Haynes' work.

model it was assigned the appropriate electron density. For the model state with elliptical cross section (state 3) the logical criterion used to assign electron density values to each point in the rotated space was

$$\left(|\xi_3| \le \frac{h}{2}\right) \wedge \left(\left(\left[\left(\frac{\xi_1}{A}\right)^2 + \left(\frac{\xi_2}{B}\right)^2\right]^{-\frac{1}{2}} \le 1\right) \wedge \left(\left[\left(\frac{\xi_1}{a}\right)^2 + \left(\frac{\xi_2}{b}\right)^2\right]^{-\frac{1}{2}} \ge 1\right)\right)$$
$$\Leftrightarrow \rho(\xi_1', \xi_2', \xi_3') = \rho_{carbon} \tag{7}$$

$$\left(|\xi_3| \le \frac{h}{2}\right) \wedge \left(\left(\left[\left(\frac{\xi_1}{a}\right)^2 + \left(\frac{\xi_2}{b}\right)^2\right]^{-\frac{1}{2}} \le 1\right) \wedge \left(\left[\left(\frac{\xi_1}{a}\right)^2 + \left(\frac{\xi_2}{b}\right)^2 + \left(\frac{\xi_3 - \frac{h}{2}}{b}\right)^2\right] \ge 1\right)\right)$$
$$\Leftrightarrow \rho(\xi_1', \xi_2', \xi_3') = \rho_{water}.$$

If both sentential forms had false truth values the point was assigned an electron density of zero. In the equations above A, B, a, and b represent the semi-major and semi-minor axes of the outer and inner ellipses respectively that bound the distorted annular CNT cross section. The values of these axes were found by the implementation of an optimization algorithm with the circumference as the target function. The circumferences of the inner and outer ellipses were assumed equal to the circumferences of the inner and outer circles that bound the annular CNT cross section of the model state 2 representative of CNTs that underwent a uniform radial contraction after the formation of a thin liquid film. The constant electron densities ρ_{carbon} and ρ_{water} were calculated from bulk densities. The electron density ρ_{carbon} was adjusted accordingly for each model state such that the number of electrons was held constant as the cross section geometry changed.

After evaluation of the above sentential forms for each point of a rotated space the density function for a model state was specified. At this point the Fourier autocorrelation theorem was utilized to generate the autocorrelation function for the space,

$$\mathcal{P}(\vec{x}) = \mathcal{F}^{-1}\{P^2\}. \tag{8}$$

In equation 8 $\mathcal{F}^{-1}$ represents the inverse Fourier transformation and P^2 is the modulus of the electron density function Fourier transform. The outlined procedure for the generation of the electron density autocorrelation function was implemented for 500 distinct permutations of uniformly distributed Euler angles for a given CNT model state. The autocorrelation functions were then averaged, yielding $\langle \mathcal{P} \rangle$. The spaces used in these calculations had a box length of 127.5 nm and a linear point density of one point every 7.5 Å. The rotationally averaged autocorrelation function and therein the reciprocal space have radial symmetry. The radial symmetry of the reciprocal space permits integration over a trace as opposed to the entire space. The lower limit of integration was taken as the minimum scatter angle to which our experimental geometry was sensitive. The minimum scattering angle was found by measuring the scatter intensities for spherical gold nanoparticles of different sizes and comparing them to integrated analytical scatter distributions.

The proximity of the CNTs to each other was ignored in considering the shape of the SAXS distributions, or in other words it was assumed that the CNTs scatter independently of each other. Independent scattering by the CNTs causes the SAXS distribution of a single CNT to have the same shape as that of the entire ensemble. The calculations were also carried out using the average wavelength of radiation emitted from the X-ray tube. The average wavelength was calculated to be 0.4 angstroms by taking a weighted average over the emission spectrum produced by the SpekCalc software package.[32-34]

The CNT deformations used in the calculations are extrapolated from the changes in geometry observed by Rossi *et. al.*[18], who used CNTs with a patchwork wall structure. Therefore the model cross section configurations used here are an upper limit to any deformation actually present in this experiment because CNTs of longer range order were used.

The calculated results of the integrated SAXS distributions for the model CNTs with changing cross section and capillary filling shown in Figure 7 show qualitative agreement with the shape of the experimentally measured as-purchased integrated SAXS profile during condensation shown in Figure 5. The similarity between the theoretical and experimental data is taken as evidence that the CNTs and contained water in this study traverse the same sequence of states visited by those observed in reference 18 during capillary condensation. In Figure 7 the integrated scatter intensities for CNTs that change cross section but do not undergo capillary condensation also exhibit a maximum but the scatter intensity returns to its initial value in state 4. This behavior is not observed experimentally during condensation, and the series of model states is not physically attainable. The integrated scatter intensities for the CNTs of constant cross section that undergo capillary condensation show a monotonic increase in intensity. While a monotonic increase is observed in the condensation data for the functionalized sample (Figure 5) this is due to a lack of control over the degree of filling resulting in incomplete capillary condensation, i.e. condensation

stops at either state two or three in Figure 6. The differences between the calculated intensity profiles along the three different series of CNT cross sections and degrees of filling indicate that the recorded scatter signal did not arise from either water content or CNT cross section alone, but was the result of both the change in CNT cross section and water content.

Unfortunately no agreement is found when the calculated integrated scatter intensities for the CNTs of changing configuration undergoing condensation are considered in reverse order, from state 4 to state 1, and are compared with any of the scatter profiles during evaporation. The discrepancy between the calculations and scatter intensities observed during evaporation reveal that the sequence of events taking place within the samples during evaporation is not simply the same set of events observed for condensation in reverse order.

SAXS distributions are composed of at least two distinct regions, the Guinier and Porod regions[27]. The Guinier region resides about the origin of reciprocal space, and may be approximated by an exponential function that also bears Guinier's name. The Guinier approximation depends on the radius of gyration of the scatterer. Therefore, the Guinier region contains information about the shape and size of the sample particles. The Porod region occupies higher spatial frequencies of reciprocal space, and is defined as the region of the distribution that asymptotically decays as $|\vec{q}|^{-4}$. There exists an approximation of the Porod region that depends on the specific surface area of the sample particles. By plotting a SAXS distribution on a log-log (base 10) plot the Guinier and Porod regions may be identified. The Porod region will have a slope of -4, and the Guinier region will lie closer to the origin of reciprocal space and possess a slope smaller than that of the Porod region. Figure 8 shows a log-log plot for one of the calculated SAXS distributions with the Porod region indicated by the appropriate straight line fit. The shaded area in Figure 8 indicates spatial frequencies probed by the experiment. From Figure 8 it is easily seen that the experiment is only sensitive to changes within the Porod region of the distribution, implying that the change in scatter signal is more readily correlated to changes in the number and nature of interfaces within the sample than it is to changes in sample shape. The Porod region of a SAXS distribution is unaffected by the particle density of the sample,[27] so the restriction of experimental sensitivity to this region legitimizes the use of a SAXS distribution
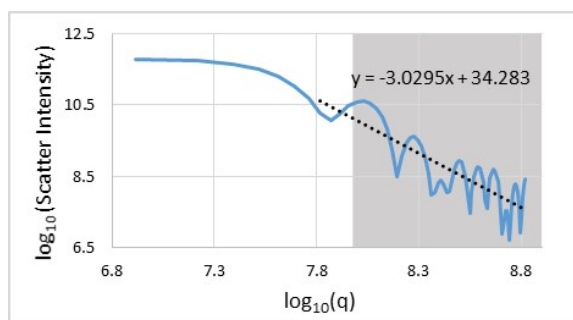

Figure 8. A trace of the SAXS distribution for an empty CNT of circular cross section (State 1 Figure 6) along one of the coordinate axes of reciprocal space is plotted on a log-log scale. The straight line fit indicates the location of the Porod region of the SAXS distribution. The shaded region marks the spatial frequencies that were probed in the experiment. The minimum scatter angle probed corresponds to radiation scattered a horizontal distance approximately equal to a single line pair of the grid projection. The slope of straight line fit to the Porod region is not equal to -4 because the size of the space used in the numerical calculations was limited by computational cost.

for a single CNT to be representative of the distribution for the entire sample to within a numerical constant.

The discrepancy between the integrated scatter profiles for evaporation and condensation could arise from a state visited by the CNTs during evaporation that is not visited during condensation, or bubbles could form during evaporation. Consider evaporation of water from the CNTs by starting at state 4 in Figure 6. The CNTs would be filled with water, and as water begins to evaporate the CNTs take on an elliptical cross section in state 3 causing an increase in scatter. If bubbles were to form on a time scale shorter than that of evaporation there would be an increase in the number of interfaces within the sample at constant mass. The generation of new interfaces would affect the sample specific surface area and therein potentially produce a second increase in scatter similar to that observed in this study.

The Kelvin equation was used to calculate the boiling point of approximately 30 °C for water confined to the inner pore of the CNTs used in this experiment. The change in CNT cross section was ignored in this calculation taking the meniscus to be hemispherical with a radius of curvature equal to 3.5 nm, meaning the contact angle was assumed to be zero. Because the Kelvin equation is an equilibrium thermodynamic expression the vapor pressure above the meniscus had to be calculated as a function of the vapor pressure above a planar surface and the surface tension

$$P(T) = (P_o(T), \gamma(T)). \qquad (9)$$

The vapor pressure above a planar meniscus is P_o, and the surface tension is γ, both of which are temperature dependent. The vapor pressure above a planar surface of water was calculated using the Antoine equation

$$log_{10}P_o = A - \frac{B}{C+T}. \qquad (10)$$

A, B, and C are empirical constants taken to have values 6.20963, 2354.731, and 7.559[35] respectively and T is the temperature in Kelvin. The temperature dependent surface tension was calculated using the equation[36]

$$\gamma(T) = B\left(1 - \frac{T}{T_c}\right)^{\mu}\left[1 + b\left(1 - \frac{T}{T_c}\right)\right]. \qquad (11)$$

B, μ, and b are empirical constants taken to have values 235.8×10^{-3} N/m, 1.256, and -0.625[36] respectively. The critical temperature for water is denoted T_c and has the value 647.15 K.

For calculation of the boiling point the pressure inside the glass vials containing the CNTs was assumed equal to that of water vapor pressure at 25 °C[35], so the temperature at which the vapor pressure above the meniscus was equal to the vapor pressure of water at 25 °C was taken as the boiling point for water confined by the CNTs. The predicted boiling point coincides with the change in evaporation time scales observed at different temperatures. The samples could be left for weeks at room temperature and would undergo an evaporation event when heated. An evaporation event clearly occurs at 45 °C, so the boiling point for water confined by the CNTs is somewhere between room temperature and 45 °C. Experiments were not conducted at temperatures lower than 45 °C because the time it would take for evaporation to go to completion would far exceed 50 hours. Agreement between the boiling point predicted by the Kelvin equation and the change in evaporation time scales, as well as the qualitative agreement between the theoretically calculated integrated scatter intensities and measured integrated scatter intensities during condensation of water into the as-purchased sample confirms that the jurisdiction of

thermodynamics at least loosely encompasses water confined to MWCNTs with 7nm inner diameter. The model states utilized in the theoretical calculation of the integrated scatter intensities were based upon observations made in reference 18. These observations agreed with the theoretical predictions by Everett and Haynes about the configuration of aqueous condensate formed during capillary condensation, which were predicated on thermodynamics.

Conclusions

The similarity in scatter profiles for the functionalized and as-purchased samples during evaporation of water from the inner cavity of the CNTs indicates that functionalization of the CNT surfaces only effects the relative time scale of evaporation and not the mechanism. Oxidation of the CNTs permitted permanent water adsorption onto the CNT surfaces at a temperature much higher than that observed for the as-purchased CNTs. Agreement between the calculated integrated scatter intensities and the observed shape of the integrated scatter profile during capillary condensation for the as-purchased sample strongly suggests that the progression of CNT cross section geometries and liquid volume configurations observed in reference 18 are the same as those in this experiment. Coincidence of the change in evaporation time scales with the boiling point predicted by the Kelvin equation and the qualitative agreement between the theoretical calculations and observed scatter intensity of the as-purchased sample during condensation stablishes the applicability of thermodynamics to water confined to dimensions less than 10nm. To the author's knowledge this is the first experimental verification that thermodynamics may be applied within this size regime.

The disparity between the theoretical calculations and scatter profiles recorded during evaporation reveal an absorption-desorption hysteresis. The hysteresis is thought to have its origin in either bubble formation or a CNT cross section geometry not seen during capillary condensation. Bubbles cause an isotropic X-ray scatter signal, while changes in cross section of the CNTs cause changes of the scatter signal perpendicular to the CNT axis. Thus SFHI's sensitivity to orientation could be used in combination with aligned CNTs to discern bubble formation during heating from a change in CNT cross section geometry.

Acknowledgements

Notes and references

1. M. Heuberger, M. Zach and N. D. Spencer, *Science*, 2001, **292**, 905-908.
2. L. D. Gelb, K. E. Gubbins, R. Radhakrishnan and M. Sliwinska-Bartkowiak, *Reports on Progress in Physics*, 1999, **62**, 1573-1659.
3. D. Mattia and Y. Gogotsi, *Microfluidics and Nanofluidics*, 2008, **5**, 289-305.
4. H. Sui, B. Han, J. K. Lee, P. Walian and B. K. Jap, *Nature*, 2001, **414**, 872-878.
5. A. A. Chialvo, L. Vlcek and D. R. Cole, *Journal of Physical Chemistry C*, 2012, **116**, 13904-13916.
6. P. Abgrall and N. T. Nguyen, *Analytical Chemistry*, 2008, **80**, 2326-2341.
7. R. Singhal, V. N. Mochalin, M. R. Lukatskaya, G. Friedman and Y. Gogotsi, *Scientific Reports*, 2012, **2**, 1-6.
8. F. Fornasiero, H. G. Park, J. K. Holt, M. Stadermann, C. P. Grigopoulos, A. Noy and O. Bakajin, *PNAS*, 2008, **105**, 17250-17255.
9. E. Dujardin, T. W. Ebbesen, H. Hiura and K. Tanigaki, *Science*, 1994, **265**, 1850-1852.
10. J. L. Bahr, E. T. Mickelson, M. J. Bronikowski, R. E. Smalley and J. M. Tour, *The Royal Society of Chemistry*, 2001, 193-194.
11. M. Pavese, S. Musso, S. Bianco, M. Giorcelli and N. Pugno, *Journal of Physics*, 2008, **20**, 1-7.
12. D. Ugarte, A. Chatelain and W. A. d. Heer, *Science*, 1996, **274**, 1897-1899.
13. D. Ugarte, T. Stockli, J. M. Bonard, A. Chatelain and W. A. d. Heer, *Applied Physics A*, 1998, **67**, 101-105.
14. R. C. Haddon, *Science*, 1993, **261**, 1545-1550.
15. A. H. Barber, S. R. Cohen and H. D. Wagner, *Phys. Rev.*, 2005, **71**, 1-5.
16. V. V. P. Chaban, O. V., *ASC Nano*, 2011, **5**, 5647-5655.
17. D. H. Everett and J. M. Haynes, *Journal of Colloid and Interface Science*, 1972, **38**, 125-137.
18. M. P. G. Rossi, Y.; Kornev, K. G., *Langmuir*, 2009, **25**, 2804-2810.
19. H. Wang, X. Xi, A. Kleinhammes and Y. Wu, *Science*, 2008, **322**, 80-83.
20. Y. Maniwa, H. Kataura, M. Abe, S. Suzuki, Y. Achiba, H. Kira and K. Matsuda, *Journal of the Physical Society of Japan*, 2002, **71**, 2863-2866.
21. H. Kyakuno, K. Matsuda, H. Yahiro, Y. Inami, T. Fukuoka, T. Miyata, K. Yanagi, H. Kataura, T. Saito, M. Yumura and S. Ijima, *Journal of Chemical Physics*, 2011, **134**, 244501-244514.
22. A. G. Yazicioglu, C. M. Megaridis, A. Nicholls and Y. Gogotsi, *Journal of Visualization*, 2005, **8**, 137-144.
23. C. Fernandez and G. Wider, *Advanced Techniques in Biophysics*, Springer-Verlag Berlin Heidelberg, New York 2006.
24. H. Wen, E. E. Bennett, M. M. Hegedus and S. C. Carroll, *IEEE Transactions on Medical Imaging*, 2008, **27**, 997-1002.
25. W. L. Y. R.-P. C. D. J., *Applied Physics Letters*, 2012, **100**, 1-4.
26. E. E. B. H. H. Wen, R.Kopace, A. F. Stein, V. Pai, *Optics Letters*, 2010, **35**, 1932-1934.
27. A. Guinier, *X-ray Diffraction In Crystals, Imperfect Crystals, and Amorphous Bodies*, Dover, Mineola, N.Y., 1994.
28. Y. Liu, B. Ahr, A. Linkin, G. J. Diebold and C. Rose-Petruck, *Optics Letters*, 2011, **36**, 2209-2211.
29. A. F. Stein, J. Ilavsky, R. Kopace, E. E. Bennett and H. Wen, *Optics Express*, 2010, **18**, 13271-13278.
30. D. Rand, V. Ortiz, Y. Liu, Z. Derdak, J. R. Wands, M. Taticek and C. Rose-Petruck, *Nano Letters*, 2011, **11**, 2678-2683.
31. J. G. W. W. Z. Li, Z. F. Ren, *Applied Physics A*, 2002, **74**, 397-402.
32. G. G. Poludniowski and P. M. Evans, *Med. Phys.*, 2007, **34**.
33. G. G. Poludniowski, *Med. Phys.*, 2007, **34**.
34. G. Poludniowski, G. Landry, F. Deblois, P. M. Evans and F. Verhaegen, *Phys. Med. Biol.*, 2009, **54**.
35. A. N. Gubkov, N. A. Fermor and N. I. Smirnov, *Zh. Prikl. Khim. (Leningrad)*, 1964, **37**, 2204-2210.

36.   N. B. Vargaftik, B. N. Volkov and L. D. Voljak, *J. Phys. Chem. Ref. Data*, 1983, **12**.